Experimental development and evaluation of a volume coil with slotted end-rings coil for rat MRI at 7 T

S. Solis-Najera[1], R. Martin[1], F. Vazquez[1], O. Marrufo[2], A. O. Rodriguez[3],
[1]*Departamento de Fisica, Facultad de Ciencias, UNAM, Department of Neuroimage,*
[3]*Department of Electrical Engineering, UAM Iztapalapa, DF, 09340, Mexico.*

A volume coil with squared slots-end ring was developed to attain improved sensitivity for imaging of rat's brain at 7 T. The principles of the high cavity resonator for the low-pass case and the law of Biot-Savart were used to derive a theoretical expression of the coil sensitivity. The slotted-end ring resonator showed a theoretical 2.22-fold improvement over the standard birdcage coil with similar dimensions. Numerical studies were carried out for the electromagnetic fields and specific absorption rates for our coil and a birdcage coil loaded with a saline-filled cylindrical phantom and a digital brain of a rat. An improvement of the signal-to-noise ratio (SNR) can be observed for the slotted volume coil over the birdcage regardless of the load used in the electromagnetic simulations. The specific absorption rate simulations show an important decrement for the digital brain and quite similar values with the saline solution phantom. Phantom and rat's brain images were acquired at 7 T to prove the viability of the coil design. The experimental noise figure of our coil design was four times less than the standard birdcage with similar dimensions, witch showed a 30% increase in experimental SNR. There is remarkable agreement among the theoretical, numerical and experimental sensitivity values, which all demonstrate that the coil performance for MR imaging of small rodents can be improved using slotted end-rings.

I. INTRODUCTION

In vivo imaging of mice and rats is soundly established as a component of preclinical and translational biomedical research [1-5]. The biomedical research community has recognized the unique power of magnetic resonance imaging (MRI) for in vivo measures in small animals [6]. The progress of research-dedicated MRI systems equipped with strong magnets (> 7 T) for small animal imaging has given a boost to RF technology. The RF receive coil is vital in determining high signal-to-noise ratio (SNR), and image quality increases with SNR, hence coil selection is critical for rodent MRI experiments.

Volume coils for small animal investigations with MRI are a particularly popular choice for a number of reasons [7-8]. In particular, birdcage coils have been a popular design for a number of years. This type of RF coil offers a convenient geometry because it can generate an excellent field uniformity, sensitivity, and natural ability to operate in quadrature. Additionally, they may be placed coaxially with the bore of the magnet for easy loading and unloading of rodents. The birdcage coil is still an important subject of study as shown by recent results [8-15].

The design of dedicated RF coils is key to achieving the best preclinical and experimental results for MRI. The end rings of the birdcage coil are an important design aspect as they can modify the intensity and homogeneity [7,10,13-15]. The principles of the cavity resonator proposed by Mansfield et. al. [16] offer an approach to improve the intensity and homogeneity of volume coils, with end rings composed of uniformly distributed slots forming a symmetrical distribution.

In this paper, we developed a coil design based on the RF coil reported in [17] and used for whole-body imaging of rats at 7 T. The coil designed proposed here is composed of squared slots end rings and reduced number of rungs to decrease specific absorption rate (SAR) [18]. We derived an expression of the sensitivity based on the low-pass cavity resonator and the law of Biot-Savart to investigate the coil performance, and experimentally validate this theoretical frame. This coil design is intended for MR imaging of a rodent's brain. As we understand, this is the first attempt to experimentally corroborate the volume coil performance using a specific end ring layout.

II. METHOD

A. End-rings comparison

There is an important difference between the end-rings in a standard birdcage coil and the modified design of the cavity resonator presented here. Fig. 1 shows a schematic and photograph of the coil proposed in this research.

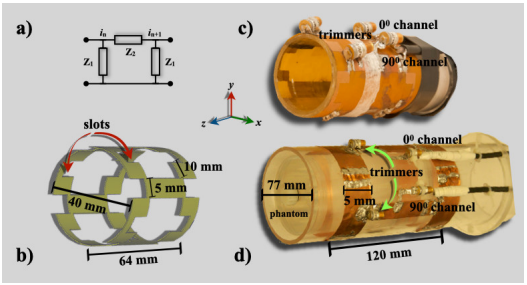

Figure 1. a) a π-section of a lumped parameter transmission line, b) schematic view of the slotted-end ring volume coil, photographs of constructed squared-slot end ring coil showing dimensions and passive electronic components (c), and birdcage coil used for comparison purposes (d).

To investigate the effect of the squared-slot end rings, we used the formalism for the physical principles of the

cavity resonator developed by Mansfield et. al. for the low-pass topology [16]. From this:

$$i^2 = i_0^2 \frac{R}{r \sum_{n=1}^{N} \cos(n\Theta)} \qquad (1)$$

where R is the rung resistance and r is the slot resistance, and $\sum_{n01}^{N} \cos(n\Theta) = \frac{N}{2}$, and

$$R = \frac{2}{Nr} Z_0^2 \qquad (2)$$

where Z_0 is the impedance of the slot, and N is the number of rungs. To compute r, we use Q, the quality factor of the low-pass cavity resonator:

$$Q = \frac{2\pi}{Nr} Z_0 \qquad (3)$$

Substituting for the resistances R, r using eqs. (2) and (3) in eq. (1), we obtain,

$$i_{\text{slot}} = i_0 \frac{Q}{\pi} \qquad (4)$$

the ratio $\frac{i_{\text{cav}}}{i_0}$ in Eq. (4) does not depend on the number of rungs, but just the quality factor.

For comparison purposes, we proceeded similarly as above, so the birdcage end rings can be studied using the intensity of the rung currents [19-20]:

$$i_{\text{bc}} = i_0 \frac{1}{2 \sin\left(\frac{\pi}{N}\right)} \qquad (5)$$

Then, combining eq. (4) and eq. (5):

$$i_{\text{slot}} = \frac{2Q}{\pi} \sin\left(\frac{\pi}{N}\right) i_{\text{bc}} \qquad (6)$$

In particular, for the 4-rung coil layout,

$$i_{\text{slot}} = 2.22\, i_{\text{bc}} \qquad (7)$$

Once we have computed the currents for the birdcage coil and the cavity resonator, we can now compare the transverse magnetic field B_1. The B_1 at the coil's isocenter relative to the end-rings current for our coil design with 4 rung is [19,20]:

$$B_{i\text{slot}} = 2.22 \frac{i_{\text{bc}} \left(l^2 + 2d^2\right)}{d \left(l^2 + d^2\right)^{3/2}} \qquad (8)$$

where l and d represent the length and the diameter of the volume coil, respectively, and Eq. (8) was computed with no shielding. A more detailed derivation of the sensitivity expression for a birdcage coil can be found in ref. [21,22].

B. Electromagnetic field simulations

The electromagnetic field simulations of RF coils can serve to guide the development of specific designs for specific applications and demonstrate how this coil design interacts with the sample to be imaged [23]. The commercial software CST Microwave Studio (CST MICROWAVE STUDIO, CST GmbH, Darmstadt, Germany) was used to calculate the electromagnetic fields. We have experimentally validated this commercial code with a birdcage coil for whole-body MRI of rats at 7 Tesla [18].

To numerically calculate the electromagnetic fields of the slotted-end rings coil, perfect electric conductors (PEC) were assumed, and together with a four-leg configuration and a saline-solution cylindrical phantom were used. The phantom properties were $\sigma = 5.55{\times}10^{-6}$ S/m, $\varepsilon = 78.4$,$\rho = 998$ kg/m^3, and $\mu = 0.999991$. A 1 V sinusoidal feed was applied, and the source and conductor impedances were set to 50 Ω (pure resistive). To calculate more realistic results, the rat's brain phantom ($\sigma = 0.527133{\times}10^{-6}$ S/m, $\varepsilon = 70$, $\rho = 1030$ kg/m^3, and $\mu = 1$) reported in [18, 24] was also used. This rat's brain model is considered a voxel-based models constructed using digital volume arrays and boundary representation (BREP) models. These type of models offer an easy implementation and fast calculation within most commercial simulation codes. [25].

A safety evaluation of RF coils is especially important to protect the sample from heat and temperature increase [26]. This is mainly done by using RF simulations in a heterogeneous body to compute realistic spatial distributions of SAR. All SAR predictions were computed assuming 1 g averaging, the IEEE STD C-95.3.1-2010 method, 1 W input power and were performed with open boundary conditions defined in all directions. Fig. 2.a) and c) show the schematic used in the corresponding numerical assessments.

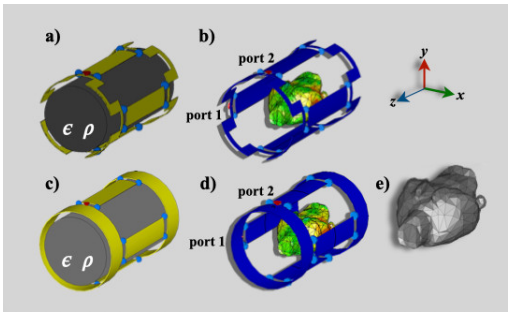

Figure 2. The simulation setups for both coils and the cylinder phantom are shown in a) and c) while the rat's digital phantom is shown in b) and d). The digital phantom used in the elecromagnetic and SAR simulations is shown in e).

The calculations were terminated after simulations of 4.23 pulse width corresponding to a system energy decay of around - 30 dB for all cases, and the duration of the excitation was around 7.11 ms. Similarly, simu-

lations were run for a birdcage with similar dimensions and the same configurations. The coils were excited in quadrature mode. The simulation setups, phantoms, and volume coils are shown in Fig. 2.b) and d).

C. Coil prototype

To optimize SNR performance, the coil dimensions should match the size of a mouse while matching the homogeneous RF region. The size of the volume coil was chosen to accommodate rats while also taking into account that a 12 cm bore was available. For this study, our coil design was 64 mm in length, 40 mm in diameter, contained four rungs, and both end rings were composed of four equally spaced rectangular slots. Fig. 1.b) and c) show a schematic and a photograph of the coil.

We designed our coil with four rungs to attenuate the SAR as experimentally shown by Martin et. al. [18]. The coil dimensions gives: diameter/length = 0.625 to avoid field homogeneity problems and to drastically affect the SNR. This result is in good concordance with ref. [12, 22]. Our coil design is a low-pass resonator because $\frac{\lambda}{20} = 50$ cm, where λ is the wavelength at 300 MHz. The RF coil prototype was built on a semi flexible printed circuit board (Pyralux®circuit flexible material: thickness = 100 μm, $\epsilon = 2.5$, $\tan(\delta) = 0.002$. Dupont™, Inc. Wilmington, DE, USA) according to the specific coil configuration. Wapler et. al. have conducted considerable investigations on a number of materials suitable to build MRI coils such as Pyralux®material [27]. This material has also been used to print coil arrays for clinical MRI [28]. This printed circuit board was mounted on an acrylic cylinder to form a volume coil.

The prototype was tuned to 299.47 MHz (the proton frequency at 7 T) using nonmagnetic chip capacitors and trimmers. One 50 Ω-coax cable was attached to each channel (0^0 and 90^0 channels) for quadrature drive, tuning and matching. Rough tuning was achieved with eleven and six fixed-value chip capacitors (American Technical Ceramics, series ATC 100 B nonmagnetic) of 3.7 pF and 3.9 pF, respectively. 50-Ω matching and fine tuning was achieved using four nonmagnetic trimmers (Voltronics, Corp: 1-33 pF, NMAJ30 0736) two for each channel. The resonant frequency for each channel was measured using a network analyzer (Model 4396A, Hewlett Packard, Agilent Technologies, CA) as the loss return (S_{11}).

After fine tuning and matching, both channels were decoupled at the desired frequencies by altering the balancing capacitor values. The quality factor (Q) of each channel in the coil was also experimentally determined by measuring the resonant frequency divided by the 3 dB bandwidth, $\Delta\omega$, with a quarter-wavelength coaxial cable at the input of the coil. The loaded Q value was measured while the coil was loaded with a saline-filled spherical phantom (3 cm diameter).

D. Imaging experiments

To test the validity of this coil, cylindrical phantom images were acquired using a standard spin echo sequence. The acquisition parameters were: TE/TR = 25 ms/900 ms, FOV = 40 mm x 40 mm, matrix size = 256 x 256, slice thickness= 2 mm, NEX = 1. Additionally, images of mouse's head were acquired using gradient echo sequence and the following acquisition parameters: TE/TR = 6 ms/400 ms, flip angle = 90^0, FOV = 35 mm x 35 mm, matrix size = 256 x 256, slice thickness = 1 mm, NEX = 1.

All MRI experiments were performed on a 7T/21cm Varian imager equipped with DirectDriveTM technology (Varian, Inc, Palo Alto, CA) and, a SGRAD 205/120/HD gradient system capable of producing pulse gradients of 400 mT/m in each of the three orthogonal axes and interfaced to a VnmrJ 2.1B console. The animal procedures were approved by the Ethical Committee of UAM Iztapalapa.

E. Noise factor

The RF penetration decreases when the coil is filled with a saline-solution phantom [7,20,22]. The noise factor (NF), is a simple way to understand the implication of this reduction. If the sample noise dominates then NF can be defined as [29]:

$$NF = 20\log_{10}\left[\frac{\mu(\mathrm{B}_1) - \sigma(\mathrm{B}_1)}{\sqrt{\frac{1}{n}\sum_s \mathrm{B}_1(x,y)}}\right] \qquad (9)$$

where $\mu(\mathrm{B}_1)$ is the mean and $\mathrm{o}(\mathrm{B}_1)$ standard deviation, n is the number of image voxels, and s is the image space.

III. RESULTS AND DISCUSSION

Our coil design was validated by full wave electromagnetic simulations, theoretical and experimental sensitivity and phantom images. To examine our coil design in more detail, electromagnetic field simulations included the electric magnetic field intensity maps of birdcage and slotted-end ring coils for the following loading cases: a) air-filled, b) saline solution-filled phantom and c) rat's digital brain phantom. Fig. 3 shows the bi-dimensional maps of the electric (E) and magnetic field (B_1) for the three cases above, and comparison plots the electromagnetic fields and SNR.

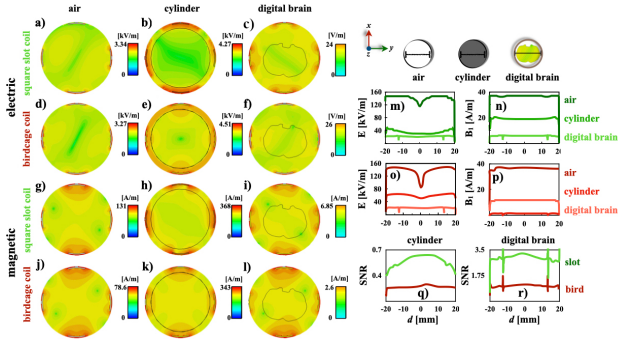

Figure 3. Series of bi-dimensional maps of the electric (a-f) and magnetic (g-l) fields for the birdcage and slotted end-ring coil. Comparison plots for E (o), B_1(p) and SNR for the saline solution (q) and the rat's brain (r) phantoms.

The bi-dimensional maps of the magnetic fields of both volume coils have very strong similarities, as shown in Fig. 3. g)-l). The simulated electromagnetic field results of both coil designs for the saline solution phantom corroborate to: a) those results reported by Webb [30], b) numerical evaluations of a band-pass-birdcage coil (ratio = 1 and 8 rungs) computed with a finite element modeling at 127.74 MHz [31], c) a quadrature low-pass birdcage coil (ratio = 0.7 and 32 rungs) obtained at 7 T for small animal MRI [32] (coil dimensions are essentially the same as ours in this study), d) numerical results obtained using the finite-difference time-domain method for a low-pass birdcage coil (ratio = 0.7 and 8 rungs) driven in quadrature mode at 7 T for rodents [33], e) a quadrature birdcage coil (ratio = 0.88 and 16 rungs) for MRI of rabbits at 7 T [34], and f) various birdcage coils (ratio = 0.62 and 8 rungs) with different rung cross sections at 9.4 T [35].

Additionally, the B_1 pattern of the saline solution simulations for both coil designs (Fig. 3.n) shows good concordance with simulations obtained at 200 MHz and 400 MHz using a simple bi-dimensional full wave model developed by Spence and Wright [36], and similar values of B_1 and field pattern were reported by Doty et. al. for a 2.5 cm Litzcage at 300 MHz [37]. The bi-dimensional representations of the electric field for both coil designs in Fig. 3.a)-c) and g)-i) are able to produce the expected behaviour as reported in [20,31]. The patterns produced by both coils are quite comparable regardless of whether the coil is filled with a phantom or not.

However, the air-filled coil case shows the best agreement. The pattern of the electric field reported by Kangarulu et. al. [38] for a transverse electromagnetic (TEM) coil with resonant frequency of 340 MHz confirms the patterns of the electric field of both coil designs in Fig. 3. m) and n). Following the simulated data of the electromagnetic fields and the methodology proposed in [39], we calculated plots of the electric field as a function of the B_1 field.

Fig. 4 illustrates the plots for the saline solution and digital brain phantoms. As expected, from this we can observe that there is a linear relation between the E and B_1, and the slope magnitudes are very similar to the experimental results obtained using an electro-optic probe at 128 MHz and 200 MHz. Another important fact is that regardless of the type of phantom used the slope value is practically the same. These experimental results validate the simulations of the electric field produced by the slotted end-ring resonator.

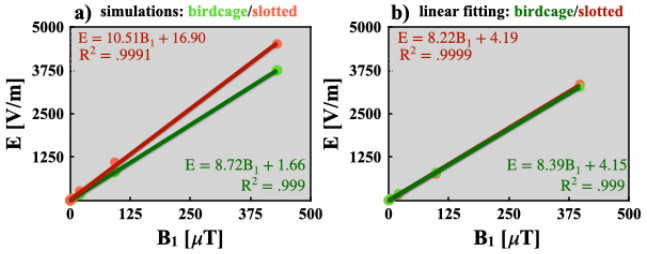

Figure 4. The linear relation between the E and B_1 magnitudes of the birdcage coil and the slotted end-ring resonator for: a) saline solution phantom and b) digital brain phantom.

Profiles of Fig. 3.m) and o) show that the electric field of the birdcage coil has a greater intensity when compared to our coil design. It is important to mention that a great deal of electrical energy was absorbed by both phantoms as shown in Fig. 3.m): when the coil is empty, the greatest energy levels were obtained, as indicated by the green profile, and for the rat's brain phantom profile, an even greater amount of energy is absorbed. The simulated SNR was computed using the bi-dimensional maps of the B_1 and E. Comparison plots were computed and shown in Fig. 3. q) and r). These SNR profiles depict a clear numerical improvement of the slotted end-ring coil over the standard birdcage coil for both cases. Numerical modeling of the interaction between the electromagnetic fields and the animal model provides a useful way to assess the rate of energy deposition. The SAR_{1g} (1 g averaging SAR) numerical assessments for the saline solution and digital brain phantoms are shown in Fig. 5.

Additionally, to compare the SAR_{1g} results, comparison histograms and profiles were obtained for the both phantoms and the standard orientations. The SAR_{1g} bi-dimensional maps of Fig. 5.a)-f) show a very good concordance with bi-dimensional maps of SAR obtained via B_1 mapping of a quadrature birdcage coil (diameter 60 cm) loaded with solution-filled cylinders at 64 MHz T [40]. These SAR_{1g} predictions in the axial (Fig. 5.a) and d)) and the coronal (Fig. 5.b) and e)) orientations agree very well with results obtained via the tomographic method and a birdcage coil (ratio = 0.91 and 16 rungs) tuned a 128 MHz [41] as well as phantom imaging studies conducted by Cline et. al. [42].

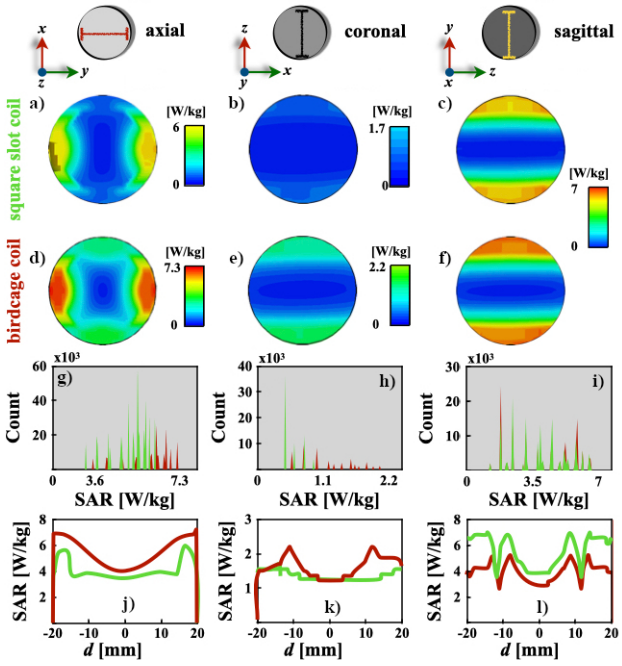

Figure 5. Series of bi-dimensional maps of SAR_{1g} for the two volume coils (a)-(f). Simulation data were used to compute for comparison histograms (g)-(i) and SAR_{1g} plots (j)-(l) as indicated in the top row illustrations.

There is a reasonable agreement between the theoretical results published by Hoult for a quadrature-driven volume coil at 200 MHz [43], and the comparison plot for axial orientation of Fig. 5.j). Histograms in Fig. 5.g)-i) show that the birdcage coil has a distribution with higher values of SAR_{1g} compared to our coil design for all three directions. The coronal cut histogram of Fig. 5.g) has a wider distribution of significantly higher values for the birdcage coil, and the slotted end-ring coil has a much lower rate of absorbed energy for the same interval. Fig. 5.h) shows that the absorbed energy ratio by the slotted volume coil is less than 1.1 W/kg, and the birdcage coil shows higher values for a wider interval approximately between 0.55 and 2 W/kg. The Fig. 4.i) distribution of energy absorbed rate by the phantom looks roughly the same along the same interval, which is confirmed by the comparison plot in Fig. 5.l). Comparison plots of SAR_{1g} in Fig. 5.j)-l) show practically the same pattern and intensity for both coil designs. edit: However, the birdcage coil shows a slight increase over the slotted end-ring coil in the axial and sagittal orientations; see Fig. 5.j) and l). This is more easily appreciated at both ends, while towards the centre, the SAR_{1g} intensity tends to be roughly the same. Similarly, numerical assessments of SAR_{1g} for the rat's digital brain phantom were computed to obtain more realistic results.

Fig. 6 shows results of SAR_{1g} for three different orientations. These bi-dimensional maps correspond very well with simulated (100 mg averaging) SAR_{100mg} predictions reported by Martin et. al. [18]. The SAR_{1g} intensity values agree with results reported by Wang et. al. [44], which assumes electromagnetic plane waves and uses the (Finite-Difference Time-Domain) FDTD method.

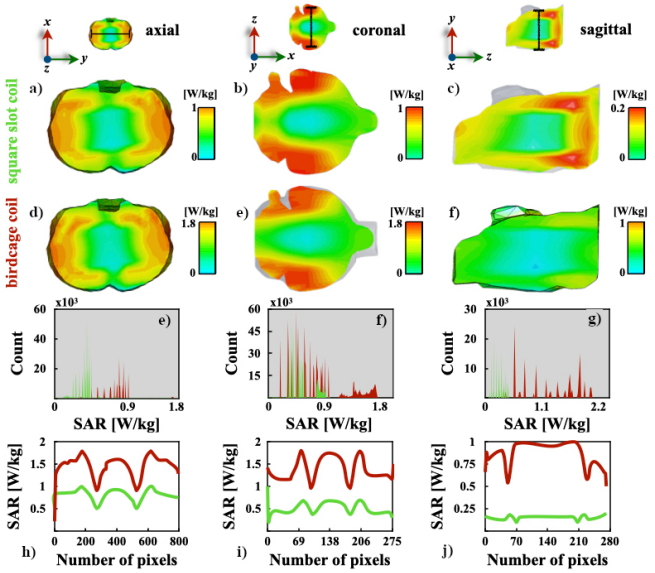

Figure 6. Series of bi-dimensional maps of SAR_{1g} for the two volume coils (a)-(f). Simulation data were used to compute for comparison histograms (g)-(i) and SAR_{1g} plots (k)-(l).

The SAR_{1g} and absorbed power results obtained from simulations in Fig. 6 are summarised in Table 1.

	Birdcage coil		**Slotted-end ring coil**	
Phantom type/SAR_{1g}	Saline solution	Digital brain	Saline solution	Digital brain
Absorbed power [mW]	179.30	9.45	147.45	3.66
total SAR_{1g} [W/kg]	2.99	1.20	2.46	0.46
maxSAR_{1g} [W/kg]	7.95	1.79	8.22	0.51
maxSAR_{1g}/total SAR_{1g}	2.65	1.49	3.34	1.10
maxSAR_{1g} location (x,y,z) [mm]	(0.42, -16.50, 17)	(13.15, -1.26, 26)	(0.46, -16.51, 47.33)	(-3.25, -8.37, 15.61)

Table 1. Comparison of SAR_{1g} results and the locations of maxSAR_{1g}

SAR_{1g} predictions of the rat's brain phantom for the slotted volume coil are lower than 0.5 W/kg in the axial

and sagittal orientations as shown in histograms of Fig. 6.e) and g). In the coronal cut of Fig. 6.f), the SAR_{1g} values are lower than 0.9 W/kg, and the birdcage coil produces a higher ratio for the entire interval. Comparison plots of Fig. 6.h)-j) clearly show lower SAR_{1g} values of the slotted volume coil than the ones obtained with the birdcage coil for all three cuts. However, the highest difference is in the saggital direction as illustrated in Fig. 6.j). The simulated absorbed power values of both coil are in reasonable concordance with the theoretical values for coil radii: $r_{\text{slotted}} = 2.28$ cm and $r_{\text{birdcage}} = 2.58$ cm, obtained with the analytical model of birdcage resonators at similar resonant frequencies and reported by Foo et. al. [45]. The SAR_{1g} bi-dimensional mappings of Fig. 6.a)-f) and their corresponding histograms (Fig. 6.e)-g) confirm the simulated results obtained with a digital anatomical model of the Sprague-Dawley rat (voxel dimension $1.95\,\text{x}\,1.95\,\mathbf{x}\,2.15\,\text{mm}^3$), based on MRI data and the FDTD numerical approach [46]. These calculations show that the slotted volume coil has better agreement with this analytical model despite our brain model having a much lower resolution ($0.18 \times 0.18 \times 0.5\,\text{mm}^3$) [18].

Greater power absorption can be observed for the saline solution phantom when compared to the digital brain phantom for both coils: an approximately 19-fold (birdcage coil) and 40-fold (slotted volume coil) increase. So, the slotted volume coil is able to absorb four times more energy than the birdcage coil. As expected, the use of digital phantoms of specific organs provide more realistic results, despite the fact that our BREP brain phantom is not able to reproduce accurately complex anatomical details. The numerical assessments of the saline solution phantom SAR_{1g} are practically the same for both coil designs. This is expected because both coil designs have similar topologies. However, the slotted volume coil produces a much lower SAR_{1g} value when using the digital brain phantom. Something very similar happens for the maxSAR_{1g} calculations which are also in good agreement with values obtained using a probabilistic approach [47]. From the maxSAR_{1g} results, we can observe that both coils have roughly the same values for the saline solution phantom, and when the digital brain model was used as a load, a 3.5-fold increase was produced. These maxSAR_{1g} computations corroborate very well with those computed by Trakic et. al. [48] using a Sprague Dawley rat model and a birdcage resonator (ratio = 1) operating at 500 MHz. The location of maxSAR_{1g} values are in the same quadrant with exception of the case for the slotted volume coil and the digital brain phantom.

The noise figures of both coil prototypes were computed according to eq. (9), giving $NF_{\text{slot}} \approx 1$, and $NF_{\text{bc}} \approx 4$. These two noise figure values have an adequate concordance with those theoretical results for half birdcage and U-shaped split birdcage resonators reported by Gasson et. al. [29]. This important reduction of NF: $NF_{\text{bird}} \approx 4NF_{\text{slot}}$, is due to the size of the birdcage resonator and eq. (8).

To characterise our coil design, the S-parameters and the Smith chart were experimentally measured. The S-parameter plots and Smith charts of both channels are in Fig. 7. Additionally, S_{11}, S_{12} and S_{21} parameters were numerically and experimentally computed for the slotted volume coil of Fig. 1.c). This S-parameter comparison has a major concordance between numerical simulations and experimental bench testings. Thus, reliable conditions can be obtained to guide the design of new RF resonators [18, 49].

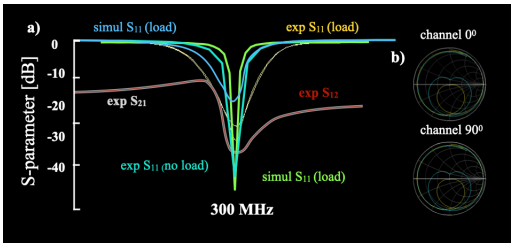

Figure 7. a) S-parameters of the slotted volume coil comparison before and after loading for the simulation and experimental case. b) Smith charts under the same conditions as in (a): blue line with load and yellow line without load.

Both channels showed a good RF penetration and impedance values. Impedance values are in good agreement with values reported by [50] and provides an optimal energy transfer. These parameters show a value lower than -20 dB, confirming a good 50-Ω match and low decoupling between the two channels to drive the coil in quadrature mode [30]. So, these S_{11}-parameters profiles show a good isolation of both channels to assure optimal energy transmission and reception of the RF signals. These results are in very good agreement with those reported in [22]. All the bench testing results are summarised in Table 2.

channel	Q factor	RF penetration [dB]	Impedance [Ω]
loaded/unloaded			
0^0	9.6/12.49	-35.84/-44.63	51.42/49.69
90^0	8.1/11.9	-38.63/-40.95	51.30/49.83

Table 2. Bench testing values for both channels of our volume coil prototype.

These Q values are in very good concordance with those reported by Marrufo et. al. [18]. The slotted end-ring coil shows a slightly better performance than a similar coil previously published with larger dimensions [17].

Phantom and rat's head images were also acquired: Fig. 8.a) and b) shows a comparison of axial images of the spherical phantom acquired with a birdcage coil and our coil, respectively. Profiles of B_1 magnitude were computed using the simulation, theoretical (Eq. (8)) and experimental results, and a comparison plot was computed, see Fig. 8.d). Comparison of uniformity and histograms for both constructed coils were also calculated

using the image data of Fig. 8.a) and shown in Fig. 8.e) and c). All profiles produced an important concordance to experimentally validate the simulation and theoretical results. The profile patterns also show an excellent agreement with those reported for a birdcage coil tuned and matched to 128 MHz [51].

The histogram of the slotted end-ring coil clearly shows a better performance over the traditional birdcage coil.

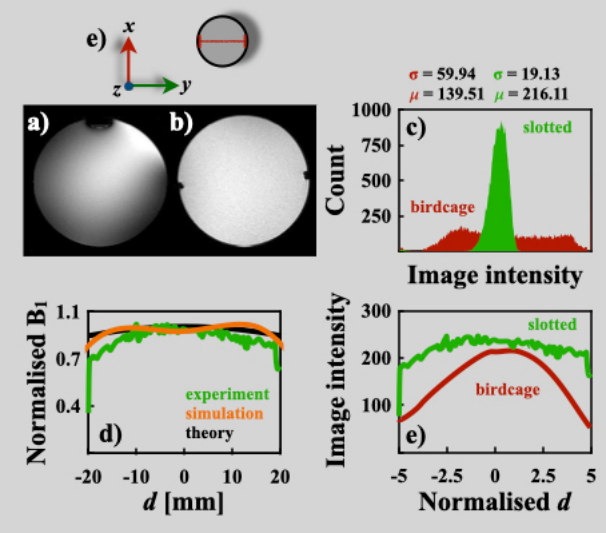

Figure 8. Phantom images: (a) birdcage coil (in-plane resolution = 312.5 μm x 312.5 μm x 1 mm^3) and, (b) slotted end-ring resonator (in-plane resolution = 117.2 μm x 117.2 μm x 1 mm^3), c) comparison of uniformity plot for simulation, theoretical and experimental results, and d) comparison of experimental data for the birdcage coil prototype of Fig. 1.d) and the slotted end-ring coil. All profiles were taken along the red line in (e).

The SNRs were also calculated using the image data of Fig. 8.a) and b). The SNR values for the coils were approximately 23 (slotted end-rings coil) and 17.6 (birdcage coil). The coil design proposed here is able to produce a reasonable improvement on performance over a standard birdcage coil. Consequently, the phantom image acquired with our coil prototype shows a better quality image and good uniformity compared to the image obtained with the birdcage coil. Successful ex vivo results of a rat's brain were obtained with our volume coil prototype at 300 MHz and shown in Fig. 9. These images of the Wistar rat head show specific brain structures with a high signal intensity, excellent image uniformity, and no movement artifacts. The phantom and rat's head images prove the compatibility of the slotted end-ring resonator with standard pulse sequences at 300 MHz.

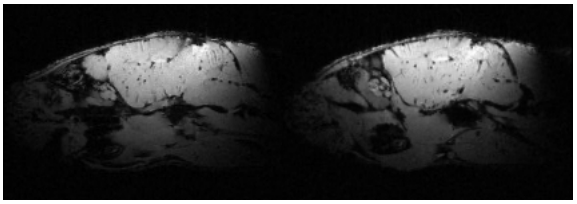

Figure 9. In vivo measurements (in-plane resolution = 117.2 μm x 117.2 μm x 1 mm^3) using the slotted end-ring coil and standard spin echo sequences. The anatomical structures of the rat's brain can be clearly identified.

IV. CONCLUSION

An RF volume coil with a slotted end-ring was presented. The important parameters of this coil prototype have been calculated analytically and numerically, and confirmed experimentally on the bench and with the MRI. The slotted end-ring coil demonstrates better coil performance than the birdcage coil in terms of sensitivity, homogeneity, SNR and SAR reduction. We have demonstrated that using full-wave electromagnetic simulations and experiments in the Varian 7 T MR imager, the slotted end-ring coil can outperform the birdcage resonator for MRI of small rodents. This can prove to be advantageous when performing functional MRI of rats' brain where the coil performance plays an important role in acquiring optimal MR signals.

V. ACKNOWLEDGMENTS.

We thank CONACYT Mexico for research grant 112092. We would like to thank Mr. Patrick Geeraert for English proofreading.email: arog@xanum.uam.mx.

[1] Kiessling, Fabian, and Bernd J. Pichler, eds. Small animal imaging: basics and practical guide. 2ed, Springer Science & Business Media, 2010. 10.1007/978-3-642-12945-2.

[2] Faqi, Ali S., ed. A comprehensive guide to toxicology in nonclinical drug development. 2 ed, Academic Press, 2017. doi.org/10.1016/C2015-0-00147-2.

[3] Messner, N. M., Zöllner, F. G., Kalayciyan, R., & Schad, L. R. (2014). Pre-clinical functional magnetic resonance imaging part II: the heart. Z Med Phy, 24(4), 307-322. doi.org/10.1016/j.zemedi.2014.06.008

[4] Marzola, P., Osculati, F. and Sbarbati, A., 2003. High field MRI in preclinical research. Euro Rournal Radiol, 48(2), pp.165-170. doi.org/10.1016/j.ejrad.2003.08.007.

[5] Lauber, D.T., Fülöp, A., Kovács, T., Szigeti, K., Máthé, D. and Szijártó, A., 2017. State of the art in vivo imaging techniques for laboratory animals. Lab Anim, 51(5), pp.465-478. doi.org/10.1177/0023677217695852.

[6] Koba, W., Kim, K., Lipton, M.L., Jelicks, L., Das, B., Herbst, L. and Fine, E., 2011, Imaging devices for use

in small animals. Semin Nucl Med (Vol. 41, No. 3, pp. 151-165). 10.1053/j.semnuclmed.2010.12.003

[7] J. T. Vaughan, R. Lagore, J. Tian. Detection Coils for MRS. eMagRes, 2016, Vol 5: 1363–1376. DOI 10.1002/9780470034590.emrstm1465.

[8] Dubois, M., Leroi, L., Raolison, Z., Abdeddaim, R., Antonakakis, T., de Rosny, J., Vignaud, A., Sabouroux, P., Georget, E., Larrat, B, Tayeb, G., Bonod, N., Amadon, A., Mauconduit, F., Poupon, C., Le Bihan, D., and Enoch S (2018). Kerker effect in ultrahigh-field magnetic resonance imaging. Phys Rev X, 8(3), 031083. 10.1103/PhysRevX.8.031083.

[9] Kausar, A. Z., Reutens, D. C., Weber, E., & Vegh, V. (2019). Monopole antenna array design for 3 T and 7 T magnetic resonance imaging. PloS one, 14(4), e0214637. doi.org/10.1371/ journal.pone.0214637.

[10] Kim, Y. C., Kim, H. D., Yun, B. J., & Ahmad, S. F. (2020). A Simple Analytical Solution for the Designing of the Birdcage RF Coil Used in NMR Imaging Applications. App Scie, 10(7), 2242. doi.org/10.3390/app10072242

[11] A. Nikulin, J. de Rosny, K. Haliot, B. Larrat, and A. Ourir. Opencage radio frequency coil for magnetic resonance imaging. Cite as: Appl. Phys. Lett. 114, 053503 (2019); https://doi.org/10.1063/1.5082245.

[12] Vincent, D. E., Wang, T., Magyar, T. A., Jacob, P. I., Buist, R., & Martin, M. (2017). Birdcage volume coils and magnetic resonance imaging: a simple experiment for students. J Biol Eng, 11(1), 41.doi.org/10.1186/s13036-017-0084-1.

[13] Qian C, Masad IS, Rosenberg JT, Elumalai M, Brey WW, Grant SC, Gor'kov PL. A volume birdcage coil with an adjustable sliding tuner ring for neuroimaging in high field vertical magnets: ex and in vivo applications at 21.1T. J Magn Reson. 2012 Aug;221:110-6. doi: 10.1016/j.jmr.2012.05.016.

[14] Fantasia M, Galante A, Maggiorelli F, Retico A, Fontana N, Monorchio A, Alecci M. Numerical and workbench design of 2.35 T double-tuned (1H/23Na) nested RF birdcage coils suitable for animal size MRI. IEEE Trans Med Imaging. 2020 Apr 17. doi: 10.1109/TMI.2020.2988599.

[15] Kozlov, M., Horner, M., Kainz, W., & Angelone, L. M. (2017, July). Investigating the effect of coil model losses on computational electromagnetic exposure of an ASTM phantom at 64 MHz MRI. In 2017 39th Ann Intern Conf IEEE Eng Med Biol Soc (EMBC) (pp. 1481-1484). IEEE. doi: 10.1109/EMBC.2017.8037115.

[16] P Mansfield, M McJury and P Glover. High frequency cavity resonator designs for NMR. Meas. Sci. Technol. 1 (1990) 1052-1059. iopscience.iop.org/0957-0233/1/10/010.

[17] O. Marrufo, F. Vazquez, S. E. Solis, A. O. Rodriguez, Slotted cage resonator for high field magnetic resonance imaging of rodents. J. Phys D: App Phys, 44, 155503, 2011. doi.org/10.1088/0022-3727/44/15/155503.

[18] R. Martin, J. F. Vazquez, O. Marrufo, S. E. Solis, A. Osorio, A. O. Rodriguez. SAR of a birdcage coil with variable number of rungs at 300 MHz. Meas 82, 482-489, 2016. (http://dx.doi.org/10.1016/j.measurement.2016.01.013).

[19] Giovannetti G. Birdcage coils: Equivalent capacitance and equivalent inductance. Conc Magn Reson Part B: Magn Reson Eng. 2014 ;44(2):32-8. doi.org/10.1002/cmr.b.21260.

[20] Mispelter, J., Lupu, M., & Briguet, A. (2006). NMR probeheads for biophysical and biomedical experiments: theoretical principles & practical guidelines. Imperial College Press.

[21] De Zanche, N., & Allen, P. S. (2002). Sensitivity calculations and comparisons for shielded elliptical and circular birdcage coils. Magn Reson Med, 47(2), 364-371. https://doi.org/10.1002/mrm.10039.

[22] De Zanche, N., Birdcage Volume Coil Desig, In Vaughan, J.T. and Griffiths, J.R. eds., 2012. RF coils for MRI. John Wiley & Sons.

[23] Collins, C. M., & Wang, Z. (2011). Calculation of radiofrequency electromagnetic fields and their effects in MRI of human subjects. Magn Reson Med, 65(5), 1470-1482. ISO 690. https://doi.org/10.1002/mrm.22845.

[24] Solis-Najera, S. E., Martin, R., Vazquez, F., & Rodriguez, A. O. (2015). Surface coil with reduced specific absorption rate for rat MRI at 7 T. MAGMA, 28(6), 599-608. DOI: 10.1007/s10334-015-0501-8.

[25] Xie T., and Zaidi B., Historical development and overview of computational animal models, in Zaidi, H. (2018). Computational Anatomical Animal Models: Methodological developments and research applications. Bristol, UK: IOP Publishing.

[26] Hoffmann, J., Henning, A., Giapitzakis, I. A., Scheffler, K., Shajan, G., Pohmann, R., & Avdievich, N. I. (2016). Safety testing and operational procedures for self-developed radiofrequency coils. NMR Biomed, 29(9), 1131-1144. DOI: 10.1002/mrm.20177.

[27] Wapler, M. C., Leupold, J., Dragonu, I., von Elverfeld, D., Zaitsev, M., & Wallrabe, U. (2014). Magnetic properties of materials for MR engineering, micro-MR and beyond. J Magn Reson, 242, 233-242. https://doi.org/10.1016/j.jmr.2014.02.005.

[28] Corea, J. R., Flynn, A. M., Lechêne, B., Scott, G., Reed, G. D., Shin, P. J., Lustig, M., & Arias, A. C. (2016). Screen-printed flexible MRI receive coils. Nat Commun, 7(1), 1-7. DOI: 10.1038/ncomms10839.

[29] Gasson, J., Summers, I. R., Fry, M. E., & Vennart, W. (1995). Modified birdcage coils for targeted imaging. Magn Reson Imaging, 13(7), 1003-1012. https://doi.org/10.1016/0730-725X(95)02003-C.

[30] Webb, A. G., Radiofrequency coils. (2016). Webb, A. G. Editor, Magnetic resonance technology: hardware and system component design. Royal Society of Chemistry. https://doi.org/10.1039/9781782623878-00081.

[31] Ruoff, J., Würslin, C., Graf, H., & Schick, F. (2012). Resolution adapted finite element modeling of radio frequency interactions on conductive resonant structures in MRI. Magn Reson Med, 67(5), 1444-1452. https://doi.org/10.1002/mrm.23109.

[32] Stara, R., Tiberi, G., Gabrieli, M., Buonincontri, G., Fontana, N., Monorchio, A., Costagli, M., Symms, M. R., Retico, A., & Tosetti, M. (2014). Quadrature birdcage coil with distributed capacitors for 7.0 T magnetic resonance data acquisition of small animals. Conc Magn Reson Part B: Magn Reson Eng, 44(4), 83-88. https://doi.org/10.1002/cmr.b.21271.

[33] Kim, K. N., Han, S. D., Seo, J. H., Heo, P., Yoo, D., Im, G. H., & Lee, J. H. (2017). An Asymmetric Birdcage Coil for Small-animal MR Imaging at 7T. Mag Reson Med Sci, 16(3), 253-258. https://doi.org/10.2463/mrms.tn.2016-0149.

[34] Lopez Rios, N., Pouliot, P., Papoutsis, K., Foias, A., Stikov, N., Lesage, F., Dehaes, M., & Cohen-Adad, J. (2018). Design and construction of an optimized transmit/receive hybrid birdcage resonator to improve full body images of medium-sized animals in 7T scanner. PloS one, 13(2), e0192035. https://doi.org/10.1371/journal.pone.0192035.

[35] Xu, Y., & Wen, Q. (2017). Comparison of 12 Quadrature Birdcage Coils with Different Leg Shapes at 9.4 T. Appl Mag Reson, 48(9), 901-909.

[36] Spence, D. K., & Wright, S. M. (2003). 2-D full wave solution for the analysis and design of birdcage coils. Conc Magn Reson Part B: Magn Reson Eng,18(1), 15-23. https://doi.org/10.1002/cmr.b.10075.

[37] Doty, F. D., Entzminger, G., Kulkarni, J., Pamarthy, K., & Staab, J. P. (2007). Radio frequency coil technology for small-animal MRI. NMR Biomed, 20(3), 304-325. DOI:10.1002/nbm.1149.

[38] Kangarlu, A., Tang, L., & Ibrahim, T. S. (2007). Electric field measurements and computational modeling at ultrahigh-field MRI. Mag Reson Imaging, 25(8), 1222-1226. https://doi.org/10.1016/j.mri.2007.01.115.

[39] Saniour, I., Gaborit, G., Perrier, A.L., Gillette, L., Revillod, G., Sablong, R., Duvillaret, L. and Beuf, O., 2018. Electro-optic probe for real-time assessments of RF electric field produced in an MRI scanner: Feasibility tests at 3 and 4.7 T. NMR Biomed, 31(1), p.e3849. https://doi.org/10.1002/nbm.3849

[40] Katscher, U., Voigt, T., Findeklee, C., Vernickel, P., Nehrke, K., & Doessel, O. (2009). Determination of electric conductivity and local SAR via B1 mapping. IEEE Trans Med Imaging, 28(9), 1365-1374.

[41] Kawamura, T., Saito, K., Kikuchi, S., Takahashi, M., & Ito, K. (2009). Specific absorption rate measurement of birdcage coil for 3.0-T magnetic resonance imaging system employing thermographic method. IEEE Trans Microw Theory Tech, 57(10), 2508-2514. 10.1109/TMTT.2009.2029712.

[42] Cline, H., Mallozzi, R., Li, Z., McKinnon, G., & Barber, W. (2004). Radiofrequency power deposition utilizing thermal imaging. Mag Reson Med 51(6), 1129-1137.

[43] Hoult, D. I. (2000). Sensitivity and power deposition in a high-field imaging experiment. J Magn Reson Imaging, 12(1), 46-67. https://doi.org/10.1002/1522-2586(200007)12:1<46::AID-JMRI6>3.0.CO;2-D.

[44] Wang, H. Y., Li, C. F., Yu, C., Dong, J., Zou, Y., Nie, B. B., Li, J. K., Ma, L., & Peng, R. Y. (2019). The specific absorption rate in different brain regions of rats exposed to electromagnetic plane waves. Sci Rep, 9(1), 1-13. https://doi.org/10.1038/s41598-019-49719-4

[45] Foo, T. K., Hayes, C. E., & Kang, Y. W. (1991). An analytical model for the design of RF resonators for MR body imaging. Magn Reson Med, 21(2), 165-177. DOI: 10.1002/mrm.1910210202.

[46] Gajšek, P., Ziriax, J. M., Hurt, W. D., Walters, T. J., & Mason, P. A. (2001). Predicted SAR in sprague-dawley rat as a function of permittivity values. Bioelectromagnetics, 22(6), 384-400. https://doi.org/10.1002/bem.66.

[47] Meliadò, E. F., Sbrizzi, A., van den Berg, C. A., Steensma, B. R., Luijten, P. R., & Raaijmakers, A. J. (2020). Conditional safety margins for less conservative peak local SAR assessment: A probabilistic approach. Mag Reson Med. https://doi.org/10.1002/mrm.28335.

[48] Trakic, A., Crozier, S., & Liu, F. (2004). Numerical modelling of thermal effects in rats due to high-field magnetic resonance imaging (0.5–1 GHz). Phys Med Biol, 49(24), 5547. 10.1088/0031-9155/49/24/010.

[49] Doty, F. D. (2018). Guide to simulating complex NMR probe circuits. Conc Magn Reson Part A, 47(2), e21463. DOI: 10.1002/cmr.a.21463.

[50] Peterson, D. M., Impedance Matching and Baluns, In Vaughan, J.T. and Griffiths, J.R. eds., 2012. RF coils for MRI. John Wiley & Sons.

[51] Vaughan, J. T., Adriany, G., Snyder, C. J., Tian, J., Thiel, T., Bolinger, L., Lilu, H., DelaBarre, L., & Ugurbil, K. (2004). Efficient high-frequency body coil for high-field MRI. Magn Reson Med, 52(4), 851-859. https://doi.org/10.1002/mrm.20177.